Journal of Advanced Ceramics
2020, **9**(6): 674–682
https://doi.org/10.1007/s40145-020-0403-8

ISSN 2226-4108
CN 10-1154/TQ

Research Article

Fabrication, microstructures, and optical properties of Yb:Lu_2O_3 laser ceramics from co-precipitated nano-powders

Ziyu LIU[a,b], Guido TOCI[c], Angela PIRRI[d], Barbara PATRIZI[c], Yagang FENG[a,b], Jiabei WEI[a,b], Feng WU[a,e], Zhaoxiang YANG[a], Matteo VANNINI[c], Jiang LI[a,b,*]

[a]*Key Laboratory of Transparent Opto-functional Inorganic Materials, Shanghai Institute of Ceramics, Chinese Academy of Sciences, Shanghai 201899, China*
[b]*Center of Materials Science and Optoelectronics Engineering, University of Chinese Academy of Sciences, Beijing 100049, China*
[c]*Istituto Nazionale di Ottica, Consiglio Nazionale delle Ricerche, CNR-INO, Sesto Fiorentino (Fi) 50019, Italy*
[d]*Istituto di Fisica Applicata "N. Carrara", Consiglio Nazionale delle Ricerche, CNR-IFAC, Sesto Fiorentino (Fi) 50019, Italy*
[e]*School of Material Science and Engineering, Jiangsu University, Zhenjiang 212013, China*

Received: February 5, 2020; Revised: July 2, 2020; Accepted: July 4, 2020

Abstract: The Yb:Lu_2O_3 precursor made up of spherical particles was synthesized through the co-precipitation method in the water/ethanol solvent. The 5 at% Yb:Lu_2O_3 powder is in the cubic phase after calcination at 1100 ℃ for 4 h. The powder also consists of spherical nanoparticles with the average particle and grain sizes of 96 and 49 nm, respectively. The average grain size of the pre-sintered ceramic sample is 526 nm and that of the sample by hot isostatic pressing grows to 612 nm. The 1.0 mm-thick sample has an in-line transmittance of 81.6% (theoretical value of 82.2%) at 1100 nm. The largest absorption cross-section at 976 nm is 0.96×10^{-20} cm^2 with the emission cross-section at 1033 nm of 0.92×10^{-20} cm^2 and the gain cross sections are calculated with the smallest population inversion parameter β of 0.059. The highest slope efficiency of 68.7% with the optical efficiency of 65.1% is obtained at 1033.3 nm in quasi-continuous wave (QCW) pumping. In the case of continuous wave (CW) pumping, the highest slope efficiency is 61.0% with the optical efficiency of 54.1%. The obtained laser performance indicates that Yb:Lu_2O_3 ceramics have excellent resistance to thermal load stresses, which shows great potential in high-power solid-state laser applications.

Keywords: Yb:Lu_2O_3 transparent ceramics; co-precipitated nano-powder; spectroscopic properties; laser performance; hot isostatic pressing

1 Introduction

With the improvement of compact and efficient InGaAs laser diodes (LDs) emitting at around 980 nm, Yb^{3+} ion-doped gain materials based on the direct pumping have become good candidates for high power solid-state lasers [1,2]. Yb^{3+} ion has a simple laser energy level scheme only including two manifolds, i.e., $^2F_{5/2}$ (excited level) and $^2F_{7/2}$ (ground level), leading to the absence of de-excitation channels, such as excited-state absorption, down-conversion cross-relaxation, or up-con-

* Corresponding author.
E-mail: lijiang@mail.sic.ac.cn

version. Yb^{3+} ion features a relatively small quantum defect allowing for an efficient diode pumping. It also has a broad emission band and a wide range of tunability permitting to generate short duration pulses [3–5]. Finally, the small diameter of the Yb^{3+} ion permits heavy doping of host materials without a significant reduction of the emission lifetime, and thus it becomes a very competitive dopant ion in various host materials, such as $Y_3Al_5O_{12}$ [6], sesquioxides [7], CaF_2 [8], $Lu_3Al_5O_{12}$ [9], and $Y_3Sc_xAl_{5-x}O_{12}$ [10]. Among the available hosts, a significant role is played by sesquioxides as they have a high thermal conductivity which decreases slowly with the doping concentration increasing. In particular, the thermal conductivity of Yb:Lu_2O_3 remains almost constant even under heavy doping levels because Yb^{3+} has an ionic radius and mass similar to Lu^{3+} ion. Consequently, Yb^{3+} doped Lu_2O_3 is particularly attractive [11–15]. However, it is very difficult to grow sesquioxide single crystals due to the extremely high melting point (> 2400 ℃), which makes Lu_2O_3 ceramics promising candidates [16]. Yb:Lu_2O_3 transparent ceramics were firstly fabricated by nanocrystalline technology combined with the conventional pressureless vacuum sintering method and subsequently a breakthrough in laser output was achieved [17,18]. Sanghera *et al.* [19, 20] reported the fabrication of Yb^{3+} doped Lu_2O_3 laser ceramics obtained by hot pressing of high purity co-precipitated powders and improved the optical properties by the hot isostatic pressing (HIP). Recently, some studies have reported that Yb:Lu_2O_3 transparent ceramics showed high optical quality using co-precipitated powders [21,22]. Briefly, nanocrystalline powder technology with a vacuum or controlled atmosphere sintering method makes it possible to fabricate highly transparent ceramic materials. It is the properties of nanocrystalline powders like the purity, morphologies, and particle sizes that play a crucial role in ceramic technology [23–26]. The properties of powders largely depend on the synthesized precursor during the co-precipitation process.

In our previous studies, we synthesized Yb:Lu_2O_3 nano-powders in pure water solvent and investigated the influence of precipitants [27,28]. It can be seen that the resultant precursors exhibited flake structures, indicating that the dispersity of the precursors needs to be improved. The various experimental factors during the co-precipitation process have great impacts on precursors. The importance of solvent in a precipitating reaction cannot be ignored. The influence of the mixed ethanol and water solvent on the microstructure of precursor has been demonstrated recently, which showed well dispersive precursors and nano-powders with a narrow distribution of particle size [29]. Ethanol is a very common solvent for inorganic salts in two aspects. Firstly, it is completely miscible with water; secondly, the polarity of the hydrogen–oxygen bond in ethanol is weaker than that in water. Adding a small quantity of ethanol into the mother solution may help to reduce the agglomeration degree. Besides, its low dielectric constant makes it easier to reach supersaturation in the mixed solvent than in the pure water under the same conditions [30,31].

This study focuses on Yb:Lu_2O_3 laser ceramics. We have synthesized Yb:Lu_2O_3 precursor in the ethanol/water mixed solution to obtain nano-powder with more favorable dispersity than in the pure water. Transparent ceramics were fabricated by vacuum sintering techniques along with the HIP method. The microstructures, optical, and spectroscopic properties of the 5 at% Yb:Lu_2O_3 ceramics were characterized as well as the laser performance.

2 Experimental

The commercial oxide powders including Lu_2O_3 (99.999%, Zhongkai New Materials Co., Ltd., Jining, China) and Yb_2O_3 (99.99%, Alfa Aesar, USA) were dissolved in an excess of hot nitric acid under heating and stirring. The highly concentrated Yb/Lu$(NO_3)_3$ solutions were assayed by chemical analysis. Then the mixed solution was prepared with the stoichiometric ratio of $Lu_{0.95}Yb_{0.05}(NO_3)_3$. Ammonium sulfate ($(NH_4)_2SO_4$, 99.0%, Sinopharm Chemical Reagent Co., Ltd., China) solution was added into the mixed solution as the dispersant in a certain molar ratio to the metal ions. Ethanol (99.7%, Shanghai Zhenxing, China) was used as solvent and washings. The mixture was diluted with the ethanol-water solution in a volume ratio of 1:2 and the concentration of RE^{3+} was set to be 0.2 mol/L. 1.0 mol/L analytical grade ammonium hydrogen carbonate (AHC, Aladdin, China) solution was prepared with the ultrapure deionized water as the precipitant.

During the normal striking process, AHC solution was dripped into the metal ion mixed solution with a certain precipitated rate. After stirring and aging, the products were washed with deionized water and alcohol by centrifugation for several times. Then the rinsed precursor was dried at 70 ℃ for 40 h in the oven.

After being sieved through a 200-mesh screen, the precursor was calcined at 1100 ℃ for 4 h in the air to obtain Yb:Lu_2O_3 nano-powder.

The synthesized nano-powder was uniaxially dry-pressed into ϕ18 mm pellets under about 69 MPa and subsequently cold isostatic pressed at 250 MPa. The green bodies were pre-sintered at 1500 ℃ for 2 h with subsequently HIP post-treatment at 1550 ℃ for 3 h under 150 MPa in Ar atmosphere. The HIPed ceramics were annealed at 900 ℃ for 20 h in air and then double-sided polished to 1.0 mm for further characterizations.

The differential thermal analysis and thermo-gravimetry (TG–DTA, Thermopiles EVO Π, Japan Rigaku) curves of the precursor were recorded at the heating rate of 10 ℃/min from room temperature to 1200 ℃. The compositions of the synthesized precursor and Yb:Lu_2O_3 powder were characterized by the Fourier transform infrared spectrometer (FT-IR, Bruker VERTEX 70, Ettlingen, Germany) on KBr pellet in the region of 4000–500 cm^{-1} under ambient conditions. The instrument of high-frequency infrared carbon and sulfur (CS-2000, Eltra, Germany) was used to determine the existence of SO_4^{2-}. The specific surface area (S_{BET}) of the nano-powder was measured by the nitrogen adsorption (BET, Quadrasorb SI, Micromeritics, USA). The phases of the precursor and powder were identified by the X-ray diffractometer (XRD, Model D/max2200 PC, Rigaku, Japan) with Cu Kα1 radiation (λ = 0.15418 nm) with the scanning rate of 5 (°)/min in the 2θ. The morphologies of the resultant precursor and powder, the microstructures of the thermally etched pre-sintered and HIPed ceramics were observed by the field emission scanning electron microscopy (FESEM, SU8220, Hitachi, Japan). In-line transmittance of the ceramic sample polished in double-sides with 1.0 mm thickness was evaluated by a UV–VIS–NIR spectrophotometer (Model Carry-5000, Varian, USA).

The laser performance of the Yb:Lu_2O_3 ceramic sample was tested by the experimental setup depicted in Fig. 1, which was similar to other previous laser tests on Yb materials [32,33]. The cavity is end-pumped. The sample was welded by a sheet of indium on a copper heat-sink and cooled by water at 19 ℃. It was pumped by a fiber-coupled laser diode which emits at 929.4 nm. The laser source shows a Gaussian pump intensity distribution in the region of the focal plane (i.e., waist radius around 65 μm at $1/e^2$, measured

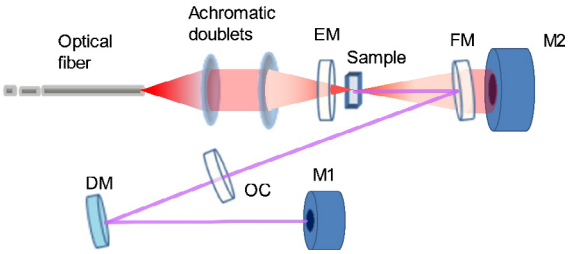

Fig. 1 Experimental laser setup.

with a CCD camera), and the numerical aperture of the pump beam is 0.22. Other elements of the cavity are: EM: End-Mirror (a flat mirror with a dichroic coating with high transmission for the pump wavelength and high reflection for the laser wavelength); FM: Folding-Mirror (a curved mirror with a curvature radius of 100 mm); OC: the flat Output Coupler mirror; M1 and M2: Power Meters, DM: Dichroic Mirror (for the rejection of the residual pump beam). The distance between FM and OC is 185 mm and that between EM and FM is 56 mm.

3 Results and discussion

All anionic groups including HCO_3^-, CO_3^{2-}, and OH^- are in the AHC solution. The floccule of lutetium carbonate would first appear when the precipitant solution is gradually added into the mixed metal solution. There exists some basic lutetium carbonate subsequently with the increasing AHC [34]. The synthesized precursor is possibly in the form of $(Lu_{0.95}Yb_{0.05})_2(OH)_{6-2x}(CO_3)_x{\cdot}nH_2O$. Moreover, the sulfur content is 0.43 wt% of the precursor according to the high-frequency infrared carbon and sulfur analysis, which demonstrates the existence of sulfate.

In order to get more details of the synthesized precursor, Fig. 2 gives the results of the TG–DTA analysis. DTA curve shows one strong endothermic peak located at 112 ℃ and the corresponding weight loss below 200 ℃ is about 14.4%, which is mainly ascribed to the evaporation of adsorbed moisture and partial molecular water. The continuing weight loss at a relatively constant rate in the range of 200–400 ℃ largely depends on the decomposition of hydroxyl and residual molecular moisture with a weight loss of 5.9%. The broad endothermic band in the range of 400–760 ℃ is mainly due to the decomposition of lutetium carbonate or basic lutetium carbonate into lutetium oxide. The approximate weight loss between 400 and

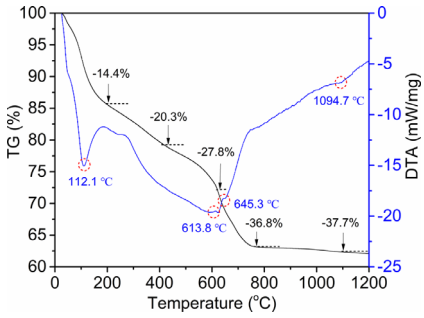

Fig. 2 TG-DTA curves of the synthesized precursor.

760 ℃ is about 16.5%. The two weak exothermic peaks in the range of 600–650 ℃ are related to the formations of Lu–O bond by stages. There is only a small loss of weight when the temperature is above 800 ℃. A few sulfates remain in the precursor as it can be seen from the weak peak at 1094 ℃. The dominant decomposition courses are depicted as follows:

$$\mathrm{Lu_{0.95}Yb_{0.05}(OH)_{3-2x}(CO_3)_x\cdot nH_2O}$$

$$\xrightarrow[\text{Dewatering}]{<200\,^{\circ}\mathrm{C}} \mathrm{Lu_{0.95}Yb_{0.05}(OH)_{3-2x}(CO_3)_x}$$

$$\xrightarrow[\text{Dehydroxylation}]{200-400\,^{\circ}\mathrm{C}} \mathrm{(Lu_{0.95}Yb_{0.05})_2O_{3-2x}(CO_3)_{2x}}$$

$$\xrightarrow[\text{Decarbonation}]{400-620\,^{\circ}\mathrm{C}} \mathrm{(Lu_{0.95}Yb_{0.05})_2O_{3-x}(CO_3)_x}$$

$$\xrightarrow[\text{Decarbonation}]{620-760\,^{\circ}\mathrm{C}} \mathrm{(Lu_{0.95}Yb_{0.05})_2O_3}$$

The total weight loss is about 37.7% when the temperature rises to 1100 ℃ chosen as the calcining temperature. The amount of the synthesized precursor is about 29 g. The obtained powder weighs about 18 g and the corresponding weight loss is about 37.9%, which is approximately equivalent to the datum from the TG-DTA analysis.

Figure 3 shows the FT-IR spectra of the synthesized precursor, which confirms the presence of OH^-, CO_3^{2-}, and SO_4^{2-} groups. The wide absorption band centered at 3387 cm^{-1} is due to the bending and stretching vibration of OH^- group. The weak peak situated at 2357 cm^{-1} results from the CO_2. The 1529 and 1403 cm^{-1} strong sharp peaks are related to the asymmetric and symmetric stretching mode of the C–O bond in CO_3^{2-} group, respectively. The weak peaks of the precursor below 850 cm^{-1} are mainly assigned to the out-of-plane deformation mode of CO_3^{2-} group. The peak located at 1083 cm^{-1} corresponds to the vibration of SO_4^{2-} [35]. For the calcined powder, the presence of weak absorption band located around 1100 cm^{-1} is related to

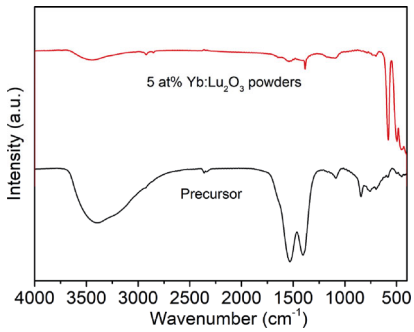

Fig. 3 FT-IR spectra of the synthesized precursor and the 5 at% Yb:Lu_2O_3 powder calcined at 1100 ℃ for 4 h.

the residual SO_4^{2-}, which can be demonstrated by the residual sulfur content of 0.17 wt% of the calcined powder. The absorption peaks of CO_3^{2-} group almost disappear. A weak absorption band around 3500 cm^{-1} demonstrates the existence of few residual hydroxyl groups, which may be ascribed to the water molecule absorbed from the air. The new sharp peak located at 580 cm^{-1} is corresponding to the Lu–O bond vibration, which is consistent with the result of DTA analysis.

According to the result of the TG–DTA analysis, the synthesized precursor was calcined at 1100 ℃ for 4 h to obtain the 5 at% Yb:Lu_2O_3 nano-powder. Figure 4 shows the experimental XRD patterns of the resultant precursor and nano-powder in comparison to the pattern of cubic Lu_2O_3 standard card PDF#12-0728. The amorphous precursor transforms into cubic Lu_2O_3 phase without any secondary phase after calcination. It demonstrates that the Yb_2O_3 is completely soluble in the Lu_2O_3. The average crystallite size (D_{XRD}) of the nano-powder is 49 nm, obtained by calculation from the full width at half maximum (FWHM) of XRD spectrum according to the Scherrer's formula [36]:

$$D_{\mathrm{XRD}} = 0.89\lambda / (\beta \cdot \cos\theta) \quad (1)$$

where λ is the wavelength of Cu Kα1 radiation, β is the FWHM of the diffraction peak at Bragg's angle (θ).

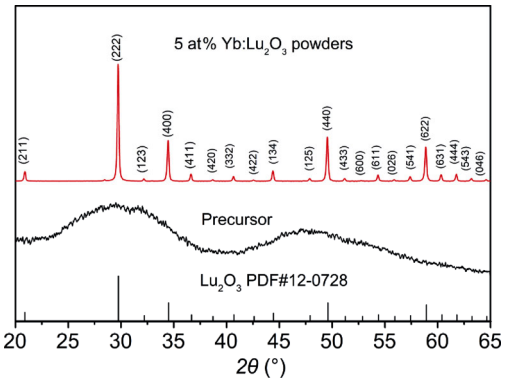

Fig. 4 XRD patterns of the synthesized precursor and 5 at% Yb:Lu_2O_3 powder calcined at 1100 ℃ for 4 h.

Figure 5 shows the FESEM micrographs of (a) the prepared precursor and (b) calcined 5 at% Yb:Lu_2O_3 nano-powder. It can be seen that the amorphous precursor consists of spherical nanogranules and shows weaker agglomeration compared to the flake structural precursors reported in our previous study [27]. The microstructure of the synthesized precursor changes greatly. This result demonstrates that the water/ethanol mixed solvent can improve the dispersivity of the precursor. Moreover, the nucleation radius of inorganic salt has a positive correlation with the dielectric constant of the solvent. The mixed solvent has a lower dielectric constant than that of the pure water, which would result in a smaller nucleation radius thus forming smaller nano-particles. In addition, the mixed solvent is expected to weaken the absorption of hydroxyl on the particle surfaces and the steric effect of ethanol may also hinder particles from moving closer to each other, which is in favor of better dispersity. The nano-powder exhibits a specific surface area (S_{BET}) of 6.626 m^2/g with an average particle size (D_{BET}) of 96 nm which is calculated according to the formula [37]:

$$D_{BET} = 6 / (\rho \cdot S_{BET}) \quad (2)$$

where ρ is 9.41 g/cm^3, the density of synthesized Yb:Lu_2O_3 powder from the XRD. Figure 5(b) shows that the nano-powder made up of spherical nanoparticles is characterized by a better dispersity after being calcined at 1100 ℃ for 4 h. Then the calcined nano-powder is dry-pressed and cold isostatically pressed to be pre-sintered in the high vacuum environment.

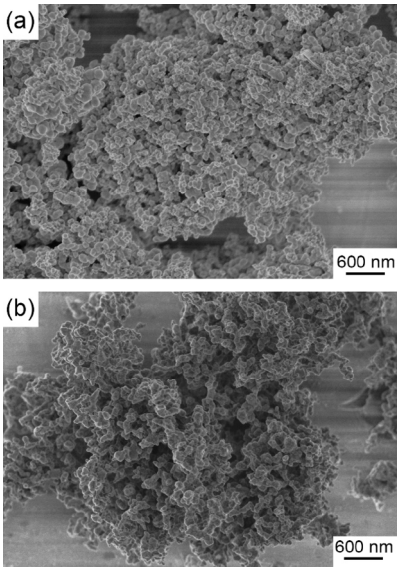

Fig. 5 FESEM micrographs of (a) the precursor and (b) the 5 at% Yb:Lu_2O_3 powder.

The opaque ceramics pre-sintered at 1500 ℃ for 2 h became transparent after HIP post-treatment at 1550 ℃ for 3 h under 150 MPa in Ar atmosphere. Then the HIPed ceramic sample was annealed at 900 ℃ for 20 h in air. After being polished on two sides, the final ceramic sample with a thickness of 1.0 mm is transparently shown in Fig. 6. The sample has an in-line optical transmittance of 81.6% (theoretic value 82.2%) at 1100 nm. However, the transmittance decreases gradually in the visible light band, i.e., 73.6% at 400 nm, lower than the theoretic value of 80.5%. Improving the optical quality in the short wavelength range will still be the key in our future studies. Briefly, the optical quality of 5 at% Yb:Lu_2O_3 ceramics is improved especially in the short wavelength range compared with the results reported in Ref. [27].

As can be seen from Fig. 7(a), a great number of large-sized micro-pores are found between the boundaries which would go against the densification of ceramics during the pre-sintering process. It possibly owes to the insufficient dispersity and uniformity of the prepared nano-powder. The ceramic sample pre-sintered at 1500 ℃ for 2 h has an average grain size of 526 nm. It is critical to increasing the relative density as much as possible to obtain transparent ceramics. A micrograph of the thermally etched surface of the HIPed ceramic sample is shown in Fig. 7(b). Compared to the surface of the pre-sintered sample, the number of micro-pores decreases greatly to thus obtain good densification and the average grain size slightly grows up to 612 nm. Therefore, the HIP conditions used here (temperature, pressure, and dwell time) are relatively well suited to reducing the porosity of the pre-sintered ceramics. The HIP approach can reduce or compress the majority of micro-pores in ceramics to improve their densification by significantly enhancing driving force [38].

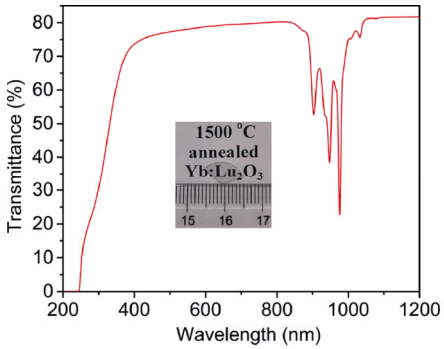

Fig. 6 In-line optical transmittance of the mirror-polished 5 at% Yb:Lu_2O_3 transparent ceramics (1.0 mm thickness) with the photograph.

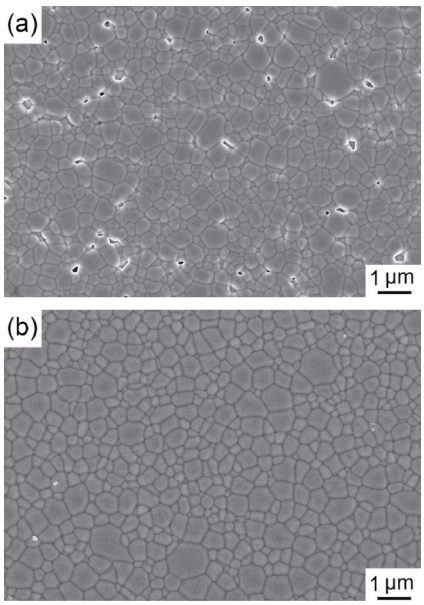

Fig. 7 FESEM micrographs of (a) the thermally etched surface of 5 at% Yb:Lu_2O_3 ceramic pre-sintered at 1500 ℃ for 2 h with (b) HIP post-treatment at 1550 ℃ for 3 h under 150 MPa.

The absorption and emission cross-sections of the final 5 at% Yb:Lu_2O_3 ceramic sample are calculated from the in-line optical transmittance, which is shown in Fig. 8(a). The absorption cross-section (σ_{abs}) is calculated by the following equations [39]:

$$n^2 = D_1 + \frac{D_2}{\lambda^2 - D_3} - D_4\lambda^2 \tag{3}$$

$$R = \frac{(1-n)^2}{(1+n)^2} \tag{4}$$

$$T = \frac{(1-R)^2\exp(-\alpha b)}{1-R^2\exp(-2\alpha b)} \tag{5}$$

$$\sigma_{abs} = \frac{\alpha}{N} \tag{6}$$

where n and λ are the refractive index and wavelength, respectively; the Sellmeier coefficients D_i (i = 1,2,3,4) are obtained from Ref. [40]; R is the Fresnel reflectivity; T is the in-line transmittance ranging from 200 to 1200 nm of the 5 at% Yb:Lu_2O_3 sample measured by the spectrophotometer; α and b are the absorption coefficient and the thickness of the sample, respectively; N is the number of the doping ions in the unit volume (1.426×10^{21} for 5 at% Yb:Lu_2O_3 ceramics). As can be seen from the absorption cross-section curve, four peaks/bands located at 903, 947, 976, and 1032 nm correspond to the $^2F_{7/2}\rightarrow{}^2F_{5/2}$ transitions of Yb^{3+}, respectively. Among these absorption lines, the former two lines possess broader linewidth, which is more suitable for laser diode pumping. The absorption cross-sections at 976 and 947 nm are 0.96×10^{-20} and 0.63×10^{-20} cm^2, respectively.

Based on the calculated absorption cross-section, the emission cross-section $\sigma_{em}(\lambda)$ can be estimated by the reciprocity method [41]:

$$\sigma_{em}(\lambda) = \sigma_{abs}(\lambda)\frac{Z_l}{Z_u}\exp\left(\frac{hc}{kT}\right)\left(\frac{1}{\lambda_{ZL}} - \frac{1}{\lambda}\right) \tag{7}$$

$$Z_a = \sum_i d_i^a \exp\left(-\frac{E_i^a}{kT}\right) \tag{8}$$

where Z_u and Z_l are the upper and lower manifold partition functions, respectively, calculated by the Eq. (8); k is the Plank constant; $a = u$ or l, d_i^a is the degeneracy of the energy level E_i^a [42] and the calculated values of Z_u and Z_l are about 1.151 and 1.227, respectively; the wavelength of the zero-phonon line, λ_{ZL}, located at 976 nm for the Yb:Lu_2O_3 ceramics; h, c, and k are the Planck constant, the light speed, and the Boltzmann constant, respectively; T is the temperature in Kelvin. Calculations are performed at room temperature (300 K). The calculated emission cross-sections at 1033 and 1079 nm are 0.92×10^{-20} and 0.28×10^{-20} cm^2, respectively. These values are very similar to those of Yb:Lu_2O_3 single crystal [42].

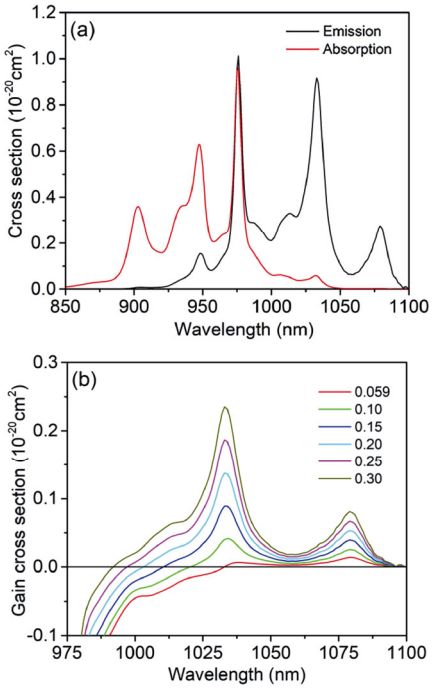

Fig. 8 (a) Absorption, emission, and (b) gain cross-sections of the 5 at% Yb:Lu_2O_3 ceramic pre-sintered at 1500 ℃ for 2 h with HIP post-treatment at 1550 ℃ for 3 h.

According to the calculated absorption and emission cross-sections, the gain cross-section can be obtained by the following equation [43]:

$$\sigma_g(\lambda) = \beta\sigma_{em}(\lambda) - (1-\beta)\sigma_{abs}(\lambda) \quad (9)$$

where σ_g is the grain cross-section; the population inversion parameter β is the fraction of the number of Yb^{3+} ions in the upper $^2F_{5/2}$ manifold to the total number of Yb^{3+} ion density. The gain cross-section as a function of the wavelength calculated with different β are shown in Fig. 8(b). The smallest β is 0.059 which is slightly higher than that of Yb:YAG ceramics (i.e., 0.055). When β is higher than 0.059, the strongest laser emission peak is located at 1033 nm. The laser wavelength at 976 nm cannot be generated because of a strong reabsorption effect.

Meanwhile, the lifetime of the upper-level $^2F_{5/2}$ of Yb^{3+} was measured using a pulsed Ti:Sapphire emitting at 895 nm (pulse duration 45 ns) for the excitation, using the so-called pinhole method to avoid radiation trapping effects [44–46]. The upper-level lifetime of 710 μs is somehow shorter than the values reported by Petermann *et al.* [47] and by Peters *et al.* [48] (820 and 805 μs, respectively).

For the laser test, the sample has a thickness of 1.0 mm and is in the shape of one-quarter of a disk with a diameter of about 13 mm. The sample has flat surfaces with a residual wedge angle of about 0.7 mrad. Several OCs with different transmission, T_{OC}, ranging from about 2% to 38% were used to find the optimal output coupling transmission. Two different campaigns of measurements were performed. In the first run, the sample was pumped in quasi-continuous wave (QCW) (10 Hz, duty factor of 20%) regime while in the second run, it was tested in the CW regime. The maximum pump power was 22.5 and 19.5 W in QCW and CW pumping conditions, respectively. The unsaturated absorption of the sample was about 17% of the incident pump power.

The QCW laser output power versus the absorbed pump power obtained with OC mirrors with different T_{OC} are shown in Fig. 9(a). The highest slope efficiency η = 68.7% with an optical efficiency of 65.1% is achieved at 1033.3 nm by T_{OC} = 18.6% and the maximum output power is 2.9 W.

CW laser test was carried out by closing the laser cavity with two OC mirrors having a transmission of 10.0% and 18.6%. As shown in Fig. 9(b), we found that the best laser performance was achieved by T_{OC} = 18.6%. At 1033 nm, laser gives about 2.3 W with a corresponding slope efficiency of 61.0% and optical

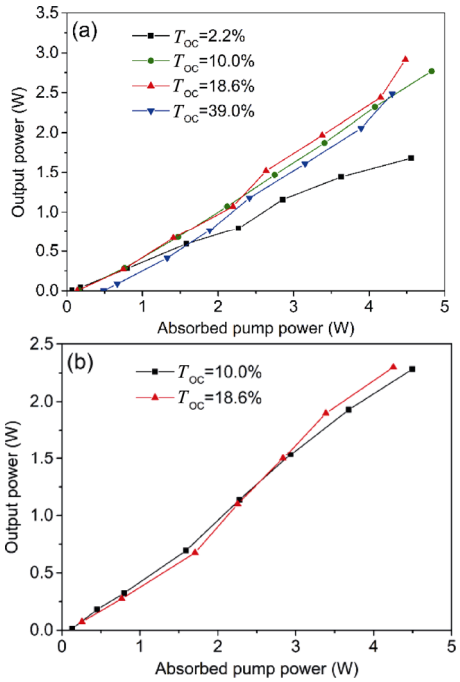

Fig. 9 Output power verse absorbed pump power obtained with OC mirrors with the different T_{OC} in *Q*CW and CW pumping conditions, respectively.

efficiency of 54.1%. It is worth noting that the slope efficiencies in the CW pumping regime are only slightly lower than those obtained in the QCW regime. This can be interpreted as a clear indication that Yb:Lu_2O_3 ceramic is very resistant to thermal stress.

The slope efficiency data obtained in QCW condition was analyzed using the Caird formula [49]:

$$\eta_L = \eta_P \frac{\lambda_P}{\lambda_L} \frac{\ln(1-T_{OC})}{\ln\left[(1-T_{OC})(1-L)\right]} \quad (10)$$

where η_L is the slope efficiency, λ_P and λ_L are the pump and lasing wavelength, respectively, to evaluate the intracavity nonsaturable loss L (here mainly due to the internal scattering in the ceramic sample) and the pumping efficiency η_P. The intracavity roundtrip loss is about 1.7%, whereas the η_P is 80%. The value of the intracavity loss is quite low, which confirms the high optical quality of the sample. The pumping efficiency is lower than unity, indicating the existence of some energy loss channel from the upper laser level. This is consistent with the observation that the upper level lifetime is shorter than the value commonly observed in crystals, as noted above.

4 Conclusions

Yb:Lu_2O_3 precursor with spherical particles has been

synthesized in the ethanol/water mixed solvent. The nano-powder calcined at 1100 ℃ for 4 h shows the average particle and grain sizes of 96 and 49 nm, respectively. The 5 at% Yb:Lu_2O_3 transparent ceramics with the grain size of 612 nm were fabricated by vacuum sintering at 1500 ℃ for 2 h with HIP post-treatment at 1550 ℃ for 3 h, whose in-transmittance reaches 81.6% at 1100 nm. The absorption cross-sections at 976 and 947 nm are 0.96×10^{-20} and 0.63×10^{-20} cm^2, respectively, and the calculated emission cross-sections at 1033 and 1079 nm are 0.92×10^{-20} and 0.28×10^{-20} cm^2, respectively. When the β is above 0.059, the strongest laser emission peak is located at 1033 nm according to the gain cross-sections. The highest η of 68.7% is observed in QCW condition and the η is 61% in CW condition with the same T_{OC} = 18.6%. The slope efficiency with the same OC in CW pumping regime is only slightly lower than that in QCW regime, indicating the excellent resistance of 5 at% Yb:Lu_2O_3 ceramics to thermal load stress. Yb:Lu_2O_3 transparent ceramics with high optical quality have great application potential in high-power solid-state lasers.

Acknowledgements

This study was supported by the National Key R&D Program of China (Grant No. 2017YFB0310500), the National Natural Science Foundation of China (Grant No. 61575212), and the Key Research Project of the Frontier Science of the Chinese Academy of Sciences (No. QYZDB-SSW-JSC022).

References

[1] Raybaut P, Druon F, Balembois F, *et al*. Directly diode-pumped Yb^{3+}:$SrY_4(SiO_4)_3O$ regenerative amplifier. *Opt Lett* 2003, **28**: 2195.

[2] Heuer AM, Saraceno CJ, Beil K, *et al*. Efficient OPSL-pumped mode-locked Yb: Lu_2O_3 laser with 67% optical-to-optical efficiency. *Sci Rep* 2016, **6**: 19090.

[3] Krupke WF. Ytterbium solid-state lasers. The first decade. *IEEE J Sel Top Quantum Electron* 2000, **6**: 1287–1296.

[4] Liu WP, Kou HM, Li J, *et al*. Transparent Yb:$(Lu_xSc_{1-x})_2O_3$ ceramics sintered from carbonate co-precipitated powders. *Ceram Int* 2015, **41**: 6335–6339.

[5] Guyot Y, Guzik M, Alombert-Goget G, *et al*. Assignment of Yb^{3+} energy levels in the C_2 and C_{3i} centers of Lu_2O_3 sesquioxide either as ceramics or as crystal. *J Lumin* 2016, **170**: 513–519.

[6] Dong J, Shirakawa A, Ueda KI, *et al*. Laser-diode pumped heavy-doped Yb: YAG ceramic lasers. *Opt Lett* 2007, **32**: 1890.

[7] Bagayev SN, Osipov VV, Shitov VA, *et al*. Fabrication and optical properties of Y_2O_3-based ceramics with broad emission bandwidth. *J Eur Ceram Soc* 2012, **32**: 4257–4262.

[8] Wei JB, Toci G, Pirri A, *et al*. Fabrication and property of Yb: CaF_2 laser ceramics from Co-precipitated nanopowders. *J Inorg Mater* 2019, **34**: 1341.

[9] Kaskow M, Galecki L, Jabczynski JK, *et al*. Diode-side-pumped, passively Q-switched Yb:LuAG laser. *Opt Laser Tech* 2015,73:101–104.

[10] Pirri A, Toci G, Li J, *et al*. A comprehensive characterization of a 10 at.% Yb: YSAG laser ceramic sample. *Materials* 2018, **11**: 837.

[11] Pirri A, Toci G, Vannini M. First laser oscillation and broad tunability of 1 at% Yb-doped Sc_2O_3 and Lu_2O_3 ceramics. *Opt Lett* 2011, **36**: 4284.

[12] McMillen CD, Sanjeewa LD, Moore CA, *et al*. Crystal growth and phase stability of Ln: Lu_2O_3(Ln=Ce,Pr,Nd,Sm, Eu,Tb,Dy,Ho,Er,Tm,Yb) in a higher-temperature hydrothermal regime. *J Cryst Growth* 2016, **452**: 146–150.

[13] Maksimov RN, Esposito L, Hostaša J, *et al*. Densification and phase transition of Yb-doped Lu_2O_3 nanoparticles synthesized by laser ablation. *Mater Lett* 2016, **185**: 396–398.

[14] Sanghera J, Shaw B, Kim W, *et al*. Ceramic laser materials. *Proc SPIE* 2011, **7912**:79121Q-1.

[15] Gaumé R, Viana B, Vivien D, *et al*. A simple model for the prediction of thermal conductivity in pure and doped insulating crystals. *Appl Phys Lett* 2003, **83**: 1355–1357.

[16] Guzik M, Pejchal J, Yoshikawa A, *et al*. Structural investigations of Lu_2O_3 as single crystal and polycrystalline transparent ceramic. *Cryst Growth Des* 2014, **14**: 3327–3334.

[17] Takaichi K, Yagi H, Shirakawa A, *et al*. Lu_2O_3:Yb^{3+} ceramics—A novel gain material for high-power solid-state lasers. *Phys Stat Sol (a)* 2005, **202**: R1–R3.

[18] Kitajima S, Nakao H, Shirakawa A, *et al*. CW performance and temperature observation of Yb:Lu_2O_3 ceramic thin-disk laser. In *Laser Congress 2017* (ASSL, LAC). OSA Technical Digest, Optical Society of America, 2017: JM5A.32.

[19] Sanghera J, Kim W, Baker C, *et al*. Laser oscillation in hot pressed 10% Yb^{3+}:Lu_2O_3 ceramic. *Opt Mater* 2011, **33**: 670–674.

[20] Kim W, Baker C, Villalobos G, *et al*. Synthesis of high purity Yb^{3+}-doped Lu_2O_3 powder for high power solid-state lasers. *J Am Ceram Soc* 2011, **94**: 3001–3005.

[21] Yin DL, Ma J, Liu P, *et al*. Submicron-grained Yb:Lu_2O_3 transparent ceramics with lasing quality. *J Am Ceram Soc* 2019, **102**: 2587–2592.

[22] Dong LL, Ma MZ, Jing W, *et al*. Synthesis of highly sinterable Yb:Lu_2O_3 nanopowders via spray co-precipitation for transparent ceramics. *Ceram Int* 2019, **45**: 19554–19561.

[23] Wang QQ, Shi Y, Feng YG, *et al*. Spectral characteristics and laser parameters of solar pumped Cr, Nd:YAG transparent ceramics. *Chin J Lumin* 2019, **40**: 1365–1372.

[24] Li XY, Liu Q, Hu ZW, *et al*. Influence of ammonium hydrogen

carbonate to metal ions molar ratio on co-precipitated nanopowders for TGG transparent ceramics. *J Inorg Mater* 2019, **34**: 791–797.

[25] Balabanov SS, Permin DA, Rostokina EY, *et al*. Sinterability of nanopowders of terbia solid solutions with scandia, yttria, and Lutetia. *J Adv Ceram* 2018, **7**: 362–369.

[26] Dai YH, Li J, Zhang Y, *et al*. Preparation of Er,Yb:$(LaLu)_2O_3$ ceramic and its upconversion luminescent properties. *Chin J Lumin* 2018, **39**: 488–493.

[27] Liu ZY, Toci G, Pirri A, *et al*. Fabrication and laser operation of Yb:Lu_2O_3 transparent ceramics from co-precipitated nano-powders. *J Am Ceram Soc* 2019, **102**: 7491–7499.

[28] Liu Q, Li JB, Dai JW, *et al*. Fabrication, microstructure and spectroscopic properties of Yb:Lu_2O_3 transparent ceramics from co-precipitated nanopowders. *Ceram Int* 2018, **44**: 11635–11643.

[29] Wu HJ, Pan GH, Hao ZD, *et al*. Laser-quality Tm:$(Lu_{0.8}Sc_{0.2})_2O_3$ mixed sesquioxide ceramics shaped by gelcasting of well-dispersed nanopowders. *J Am Ceram Soc* 2019, **102**: 4919–4928.

[30] Chen SF, Yu SH, Yu B, *et al*. Solvent effect on mineral modification: Selective synthesis of cerium compounds by a facile solution route. *Chem Eur J* 2004, **10**: 3050–3058.

[31] Chen SF, Yu SH, Jiang J, *et al*. Polymorph discrimination of $CaCO_3$ mineral in an ethanol/water solution: Formation of complex vaterite superstructures and aragonite rods. *ChemInform* 2006, **37**: 115–122.

[32] Feng YG, Toci G, Pirri A, *et al*. Fabrication, microstructure, and optical properties of Yb:$Y_3ScAl_4O_{12}$ transparent ceramics with different doping levels. *J Am Ceram Soc* 2020, **103**: 224–234.

[33] Dai ZF, Liu Q, Toci G, *et al*. Fabrication and laser oscillation of Yb:Sc_2O_3 transparent ceramics from co-precipitated nano-powders. *J Eur Ceram Soc* 2018, **38**: 1632–1638.

[34] Cai S, Lu B, Chen HB, *et al*. Homogeneous $(Lu_{1-x}In_x)_2O_3$ (x = 0−1) solid solutions: Controlled synthesis, structure features and optical properties. *Powder Technol* 2017, **317**: 224–229.

[35] Sun ZG, Chen ZY, Wang MY, *et al*. Production and optical properties of Ce^{3+}-activated and Lu^{3+}-stabilized transparent gadolinium aluminate garnet ceramics. *J Am Ceram Soc* 2020, **103**: 809–818.

[36] Monshi A, Foroughi MR, Monshi MR. Modified scherrer equation to estimate more accurately nano-crystallite size using XRD. *World J Nano Sci Eng* 2012, **2**: 154–160.

[37] Li SS, Zhu XW, Li J, *et al.* Fabrication of 5at.%Yb:$(La_{0.1}Y_{0.9})_2O_3$ transparent ceramics by chemical precipitation and vacuum sintering. *Opt Mater* 2017, **71**: 56–61.

[38] Toci G, Hostaša J, Patrizi B, *et al*. Fabrication and laser performances of Yb:Sc_2O_3 transparent ceramics from different combination of vacuum sintering and hot isostatic pressing conditions. *J Eur Ceram Soc* 2020, **40**: 881–886.

[39] Harris DC. Materials for infrared windows and domes: properties and performance. *Opt Photonics News* 1999: 21–25.

[40] Kaminskii AA, Sh Akchurin M, Becker P, *et al*. Mechanical and optical properties of Lu_2O_3 host-ceramics for Ln^{3+} lasants. *Laser Phys Lett* 2008, **5**: 300–303.

[41] McCumber DE. Einstein relations connecting broadband emission and absorption spectra. *Phys Rev* 1964, **136**: a954.

[42] Laversenne L, Guyot Y, Goutaudier C, *et al*. Optimization of spectroscopic properties of Yb^{3+}-doped refractory sesquioxides: Cubic Y_2O_3, Lu_2O_3 and monoclinic Gd_2O_3. *Opt Mater* 2001, **16**: 475–483.

[43] Gan FX, Deng PZ. Laser Materials. Shanghai, China: Shanghai Science and Technology Press, 1996.

[44] Kühn H, Fredrich-Thornton ST, Kränkel C, *et al*. Model for the calculation of radiation trapping and description of the pinhole method. *Opt Lett* 2007, **32**: 1908–1910.

[45] Toci G. Lifetime measurements with the pinhole method in presence of radiation trapping: I—theoretical model. *Appl Phys B* 2012, **106**: 63–71.

[46] Toci G, Alderighi D, Pirri A, *et al*. Lifetime measurements with the pinhole method in presence of radiation trapping: II—application to Yb^{3+} doped ceramics and crystals. *Appl Phys B* 2012, **106**: 73–79.

[47] Petermann K, Fagundes-Peters D, Johannsen J, *et al*. Highly Yb-doped oxides for thin-disc lasers. *J Cryst Growth* 2005, **275**: 135–140.

[48] Peters R, Kränkel C, Petermann K, *et al*. Crystal growth by the heat exchanger method, spectroscopic characterization and laser operation of high-purity Yb:Lu_2O_3. *J Cryst Growth* 2008, **310**: 1934–1938.

[49] Caird JA, Payne SA, Staber PR, *et al*. Quantum electronic properties of the $Na_3/Ga_2/Li_3F_{12}:Cr^{3+}$ laser. *IEEE J Quantum Electron* 1988, **24**:1077–1099.